Exploring charge transport properties and functionality of molecule-nanoparticle ensembles

Devid, E.J.

Appendix A.1

Additional information about cotunneling regimes

To demonstrate that equation 4.2 provides a unified description of various transport regimes observed in experiments, equation 4.2 will be elaborated for several limiting cases.

Since the dependence of the cotunneling probability on the number of junctions j is exponentially strong, one can leave only the dominating term in the sum with a good accuracy (see equation 4.2). At relatively small bias voltage, $eV_{jct} < k_B T \ln(e^2 R_T/h)$, the optimal number of junctions j_{opt}, which gives the maximum contribution to the current, is smaller than $N_{max} \approx \sqrt{E_C/eV_{jct}}$. In order to find the optimal number in this case j is treated as a continuous parameter and we solve the saddle-point equation

$$\frac{\partial}{\partial j}\left[-\frac{E_C}{jk_BT} - j\, ln\frac{e^2R_T}{h} + (j-1)\ln\frac{{k_B}^2T^2+{e^2V_{jct}}^2}{{E_C}^2}\right] = 0.$$

The solution of this equation reads

$$j_{opt} = \sqrt{\frac{E_C}{k_BT\ln\left[\frac{e^2R_TE_C^2}{h\left({e^2V_{jct}}^2+{k_B}^2T^2\right)}\right]-eV_{jct}}}. \qquad \text{(S4.1)}$$

Thus the current may be approximated as follows

$$I \propto V_{jct}\left(\frac{h}{e^2R_T}\right)^{j_{opt}}\left(\frac{{k_B}^2T^2+{e^2V_{jct}}^2}{{E_C}^2}\right)^{j_{opt}-1} exp\left[-\frac{E_C}{j_{opt}k_BT}+j_{opt}\frac{eV_{jct}}{k_BT}\right]$$

$$= \frac{{E_C}^2V_{jct}}{{e^2V_{jct}}^2+{k_B}^2T^2}\, exp\left(-2\sqrt{\frac{E_C}{k_BT}\left(ln\left[\frac{e^2R_TE_C^2}{h\left({e^2V_{jct}}^2+{k_B}^2T^2\right)}\right]\right)}-\frac{eV_{jct}}{k_BT}\right). \qquad \text{(S4.2)}$$

In the linear response regime $eV_{jct} < k_BT$ the current (S4.2) reduces to the form

$$I = GV_{jct}, \qquad \text{(S4.3)}$$

where the zero-bias conductance follows an Efros-Shklovskii relation (in temperature):

$$G \propto \left(\frac{h}{e^2R_T}\right)^{N_{cot}}\left(\frac{k_BT}{E_C}\right)^{2N_{cot}-2} exp\left[-\frac{E_C}{N_{cot}k_BT}\right] = \frac{E_C^2}{{k_B}^2T^2}\, exp\left[-\sqrt{\frac{T^*}{T}}\right], \qquad \text{(S4.4)}$$

Here the characteristic temperature $k_BT^* = 4E_C\, ln\left(e^2R_TE_C^2/hk_B{}^2T^2\right)$ is introduced, and we have defined the optimal cotunneling distance at zero bias $N_{cot} = \sqrt{\frac{E_C}{k_BT\ln\left(e^2R_TE_C^2/hk_B{}^2T^2\right)}}$, which follows from equation S4.1 at V_{jct} = 0, i.e. $N_{cot} = j_{opt\,|V_{jct}=0}$. Since in practice the ratio E_C/k_BT is not extremely large, one can ignore its logarithmic contribution in the denominator and approximate N_{cot} as follows

$$N_{cot} \approx \sqrt{\frac{E_C}{k_BT\ln(e^2R_T/h)}}. \qquad \text{(S4.5)}$$

The results (equations S4.3 and S4.4) apply to the region of parameters C1 defined in the main text of the article.

At higher bias voltages, $k_BT < eV_{jct} < k_BT\ln\left(\frac{e^2R_T}{h}\right)$, the current (see equation S4.2) may be roughly approximated by a power law dependence. In order to reveal that, the combination eV_{jct} under the square root in the exponent of equation S4.2 is neglected and further is made use of the relation $\ln\left(1 + e^2V_{jct}{}^2/k_B{}^2T^2\right) \ll \ln\left(e^2R_TE_C^2/\right.$ $\left.hk_B{}^2T^2\right)$, which holds in this regime.

Afterwards, the exponent in powers of $\ln\left(1 + e^2V_{jct}{}^2/k_B{}^2T^2\right)$ is expanded and the following result arrives:

$$I \propto \frac{G}{e}\frac{\left(eV_{jct}\right)^{2N_{cot}-1}}{(k_BT)^{2N_{cot}-2}}\,. \qquad \text{(S4.6)}$$

Equation S4.6 describes the regime C2 introduced in the article.

At even higher bias voltages, when $eV_{jct} > k_BT\ln\left(\frac{e^2}{h}R_T\right)$, the optimal cotunneling distance in equation S4.1 formally exceeds the maximum allowed distance $N_{\max}$. This means that the maximum contribution to the current (S4.7) comes from the term with $j = N_{max}$. Thus, in this regime is obtained:

$$I \propto V_{jct}\left(\frac{h}{e^2R_T}\right)^{N_{max}}\left(\frac{k_B{}^2T^2+e^2V_{jct}{}^2}{E_C{}^2}\right)^{N_{max}-1} \approx \frac{E_C}{e}exp\left(-\sqrt{\frac{V^*}{V_{jct}}}\right) \qquad \text{(S4.7)}$$

where $V^* = \frac{E_C}{e}\left(\ln\frac{e^2R_TE_C}{heV_{jct}}\right)^2 \approx \frac{E_C}{e}\left(\ln\frac{e^2R_T}{h}\right)^2$ is the characteristic voltage.

Equation S4.7 corresponds to the regime C3. Interestingly, in regime C3, Efros-Shklovskii-type behaviour (in voltage) is expected.

Appendix A.2

Low-bias conductance versus temperature

Figure A-1 shows low-bias conductance versus temperature, i.e. $G(T)$, data for a quasi 2D octanethiol-gold network, plotted using different representations.

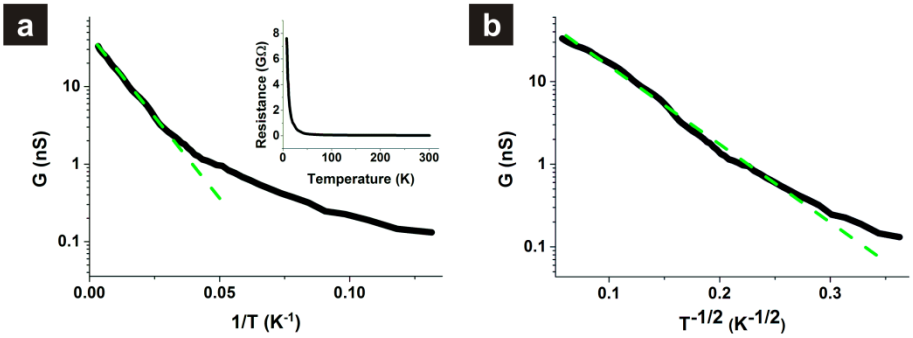

Figure A-1: (a) Arrhenius plot of conductance G versus reciprocal temperature (T^{-1}) for an octanethiol-gold nanoparticle network (see equation 4.1). The green dotted curve is a linear guide to the eye, showing the temperature range where sequential tunneling dominates. The inset shows the corresponding R versus T plot on linear axes, emphasizing the dramatic resistance increase at low temperatures (b) An Efros-Shklovskii plot of the same data as in (a). The green dotted curve is a guide to the eye (see equation 4.7). Note that at very low temperatures (< 10 K), a deviation from Efros-Shklovskii behaviour is observed.

Figure A-1(a), displays these data (see also inset) in an Arrhenius plot, based on equation 4.1. The graphs suggests that sequential tunneling dominates in the temperature range from 300 K down till roughly 50 K. At lower temperatures, however, deviations from Arrhenius behaviour are clearly observed. Figure A-1(b) shows an Efros-Shklovskii plot, based on equation 4.7. In the temperature range around 20-150 K, the data follow Efros-Shklovskii behaviour reasonably well. Hence, we find a clear indication for a crossover between sequential and cotunneling tunneling. However, the exact crossover temperature is hard to pin down as the data fit reasonably well to both types of behaviour in an extended temperature range between 50 and 150 K.

Appendix A.3

Additional data analysis

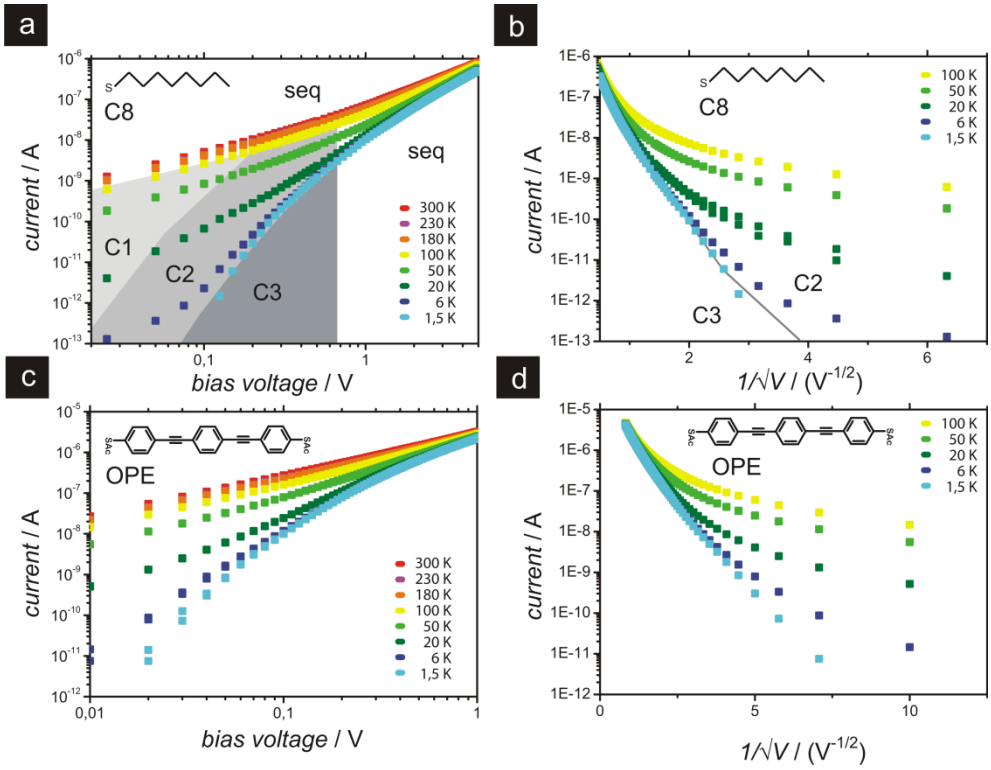

Figure A-2: *I-V* curves at several temperatures for the sample presented in the main text in Figure 4.4(a) and Figure 4.4(b) i.e. before (Figure A-2(a), (b)) and after exchange (Figure A-2(c), (d)). (a) Log-Log plot of the *I-V* curves presented in Figure 4.4(a) in the main text. In the cotunneling regime, three different signatures are observed, labelled C1 (thermally activated cotunneling), C2 (multiple inelastic cotunneling) and C3 (Efros-Shklovskii law), related to the different energy scales. In the classical and cotunneling C1 regimes, $I \propto V$ (label 1, next to the curves). In cotunneling C2 regime, $I \propto V^{\alpha}$ (with an exponent α between 1.8 and 6.2). (b) Same data presented in the form of Efros-Shklovskii plot. The gray line represents the limit below which Efros-Shklovskii field behaviour is expected. The *I-V* curves at 1.5 and 6 K are at the borderline between regimes C2 and C3. (c) Log-Log plot of the *I-V* curves presented in Figure 4.4(b) in the main text. (d) Same data presented in the form of Efros-Shklovskii plot.

In Figure A-2 we replotted the *I*-*V* data of C8-covered nanoparticles at different temperatures, reported in Figure 4.4(a) as well as the data after molecular exchange with OPE, presented in Figure 4.4(b) and on a Log-Log scale and in an Efros-Shklovskii plot, respectively. The results of Figure A-2 confirm the conclusions presented above in paragraph 4.5.

Appendix A.4

Methodology used to separate the different cotunneling regimes (C1, C2, C3) in the presented log-log plots.

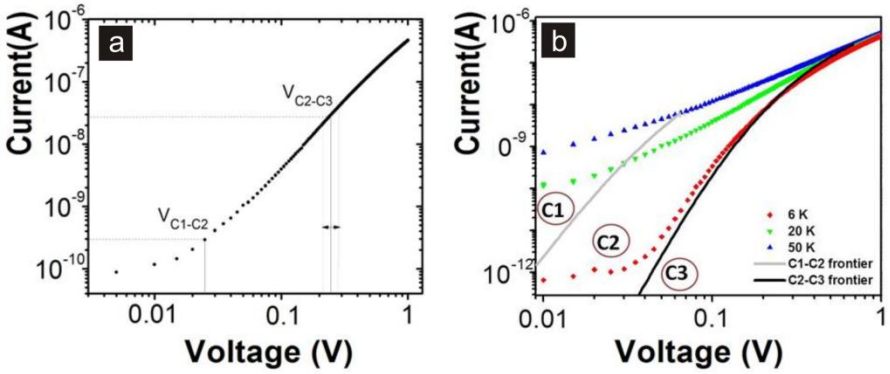

Figure A-3: (a) Example of the methodology used for estimating the current and voltage values defining the C2-C3 and C1-C2 boundaries (shown here on the *I-V* curve of the OPE sample, at 20 K). The error bar for the value of C2-C3, is related to the uncertainty in R_T. (b) Example of C2-C3 and C1-C2 boundaries construction from the points extracted 6 K, 20 K and 50 K curves.

Here the methodology is described to plot the delimitation line between regions C1 and C2, and between regions C2 and C3. For each *I-V* curve at a given temperature (see example on Figure A-3(a)) one needs to find the two points of coordinates (I_{C1-C2},V_{C1-C2}) and (I_{C2-C3},V_{C2-C3}), where V_{C1-C2} and V_{C2-C3} are related to the energy range limits of regime C2 and C3 respectively as (see equations 4.4 till 4.6): $V_{C1-C2} = \frac{Nk_BT}{e}$ and $V_{C2-C3} = \frac{Nk_BT}{e} ln\left(\frac{e^2}{h}R_T\right)$, with N is the average number of particles along an array contacting the left electrode to the right electrode (N = 15 for the particular sample studied here), and V the bias voltage applied between these two electrodes (with the bias of a single junction defined as $V_{jct} = V/N$). R_T is estimated from data of Figure 4.5, using the equation S4.5:

$$N_{cot} \approx \sqrt{\frac{E_C}{k_B T \ln(e^2 R_T/h)}}.$$

Typical values of R_T ~100 MΩ for OPE molecules and R_T ~1-5 GΩ for C8 molecules are obtained. Once $V_{C1\text{-}C2}$ and $V_{C2\text{-}C3}$ are calculated, $I_{C1\text{-}C2}$ and $I_{C2\text{-}C3}$ are extracted from each *I*-*V* curves at several temperatures.

The demarcations delimiting region C1 from C2, and region C2 from C3 are obtained by joining together all ($I_{C1\text{-}C2}$,$V_{C1\text{-}C2}$) and ($I_{C2\text{-}C3}$,$V_{C2\text{-}C3}$) points (see Figure A-3(b)).

Appendix B.1

Temperature-dependent *I-V* 's of a multilayered Au-NP-S-BPP network

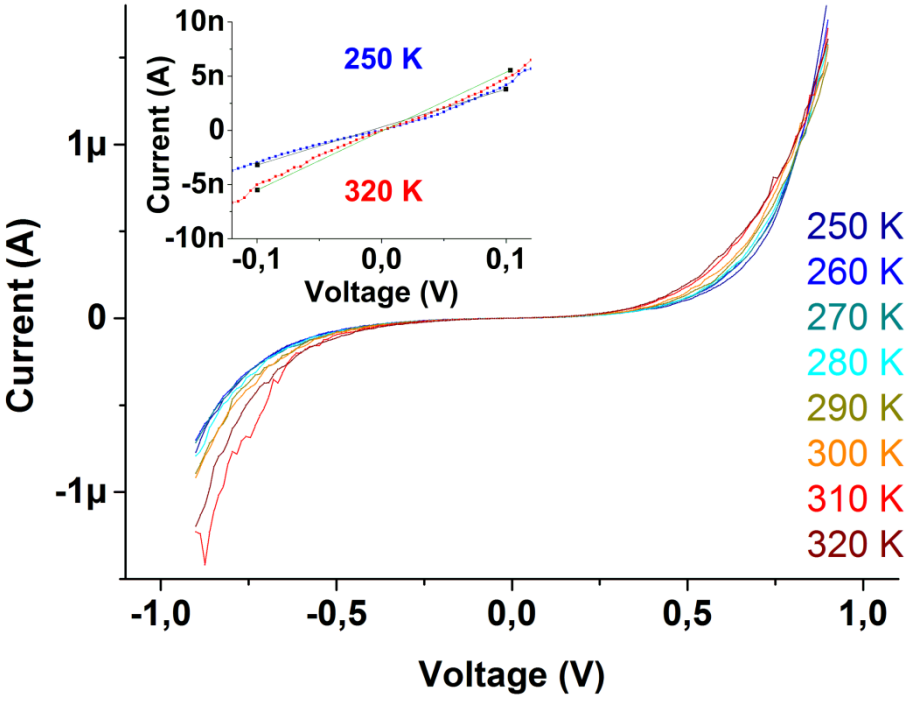

Figure B-1: Temperature-dependent *I-V* curves of a multilayered Au-NP-S-BPP network on a HAR nanotrench device. The data are taken between 250 K and 320 K (the inset zooms in at low-bias range for the *I-V* curves at 250 K and 320 K).

Appendix B.2

Modelling the charging energy of 2D Au-NP-S-BPP arrays as function of the dielectric constant

To get a feeling for the expected values of E_C for these multilayered Au-NP-S-BPP networks, the E_C is plotted in Figure B-2 as a function of the dielectric constant based on three models to approximate the E_C for a 2D Au-NP-S-BPP array.

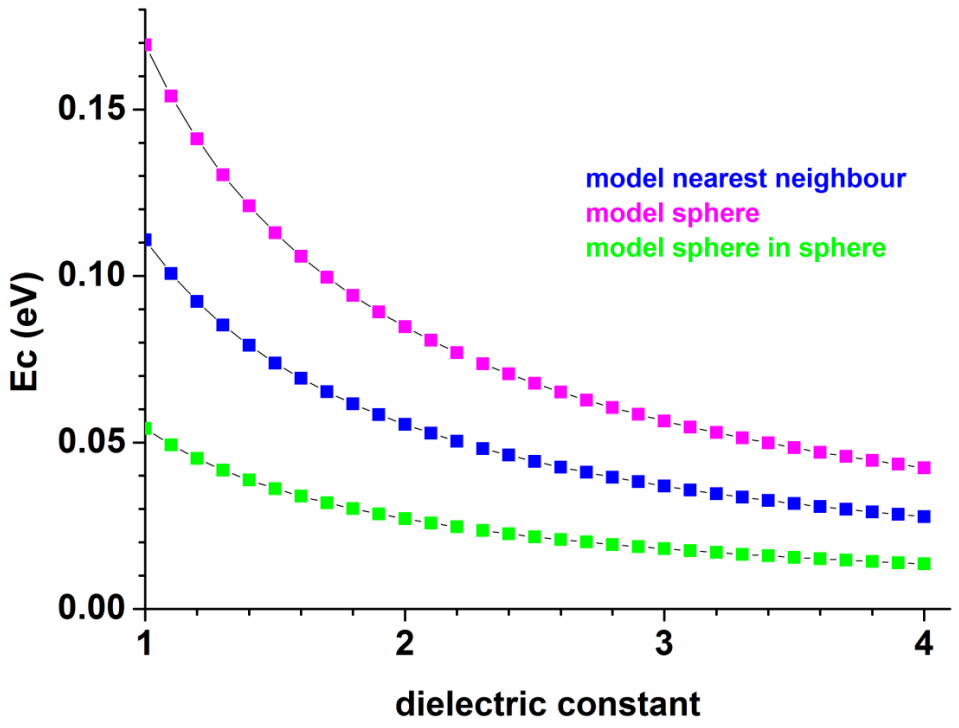

Figure B-2: E_C as function of the dielectric constant for a 2D Au-NP-S-BPP array, calculated through three different models.

The following models are used in Figure B-2 to determine the E_C of a 2D Au-NP-S-BPP array. The first model is the simple spherical model to calculate the maximum limit of E_C for a 2D Au-NP-S-BPP array (see equation S5.1)

$$E_C = \frac{e^2}{8\pi\varepsilon_0\varepsilon_r r}\,. \qquad \text{(S5.1)}$$

Where r is the radius of the gold nanoparticle in a 2D Au-NP-S-BPP array (earlier determined by TEM (see paragraph 5.4). The dielectric constant ε of a 2D Au-NP-S-BPP array (based on UV-Vis analyses, see paragraph 5.5) is set on 2.8.

The second model is called the "sphere in sphere" model which estimates a minimum limit of E_C. In the model "sphere in sphere" the total capacitance of a gold nanoparticle is calculated assuming it is fully surrounded by other gold nanoparticles. This is approximated by assuming the metallic sphere is in a second concentric metal shell [48] (see equation S5.2)

$$E_C = \frac{e^2}{\frac{8\pi\varepsilon_0\varepsilon_r}{\left(\frac{1}{r}-\frac{1}{r+d}\right)}}\,. \qquad \text{(S5.2)}$$

Where for d (i.e. the length of two entangled S-BPP molecules) 2 nm is used. The radius r remains set at 4.25 nm.

The third model is called the "nearest neighbour" model [49] (see equation S5.3)

$$E_C = \frac{e^2}{2\left([4\pi\varepsilon_0\varepsilon_r r]+\left[4\pi\varepsilon_0\varepsilon_r\frac{r^2}{d}\left(1+\frac{r^2}{d^2-2r^2}+\frac{r^4}{d^4-4d^2r^2+3r^4}\right)\right]\right)}. \qquad \text{(S5.3)}$$

Based on mirror charges between two spherical nanoparticle, this model calculates an E_C intermediate value that fits between the upper and lower E_C limits of respectively equation S5.1 and S5.2. Here r is the radius of the gold NP in 2D Au-NP-S-BPP array and d is $2r$ + 2 nm (i.e. the distance between two nanoparticles separated by S-BPP molecules with a dielectric constant of 2.8).

From Figure B-2 can be determined that for a 2D Au-NP-S-BPP array with a dielectric constant of 2.8, the E_C of 2D Au-NP-S-BPP array ranges 0.019-0.060 eV. Unfortunately, the models are rather crude or indicative. Note however that the experimental value of E_C is expected to be significantly larger for alkanethiol arrays than for Au-NP-S-BPP arrays, due to the lower dielectric constant in the alkanethiol arrays (see UV-Vis section in paragraph 5.5).

Appendix C.1

SEM image of 1'-gold nanoparticle network on nanotrench device

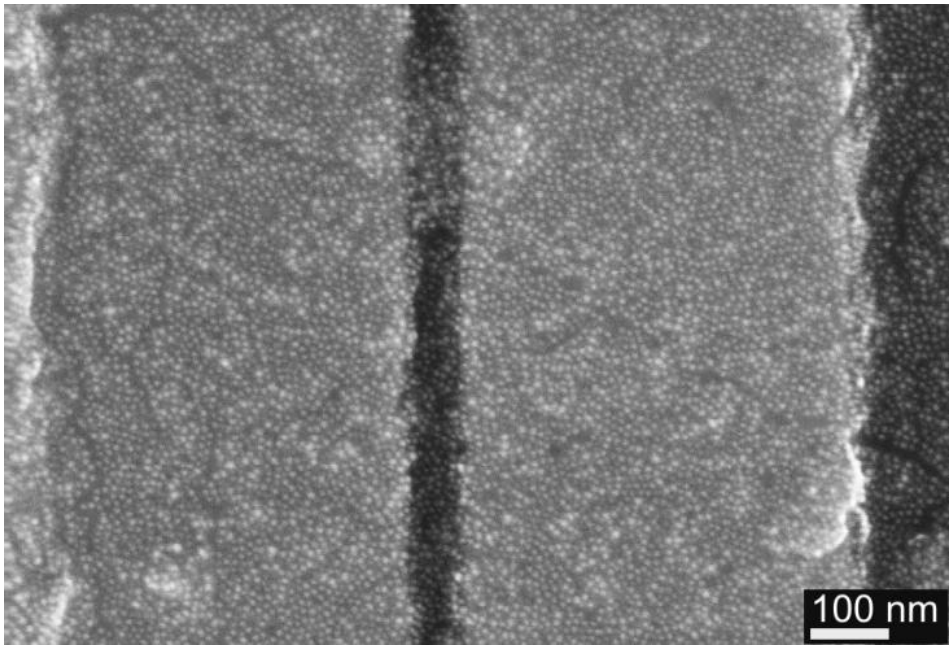

Figure C-1: SEM image of nanotrench gold electrodes device, microcontact printed with layer-on-layer C8-gold nanoparticle arrays and exchanged with **1'** molecules to obtain a layered **1'**-gold nanoparticle network.

Appendix C.2

UV-Vis measurement of C8-gold nanoparticle array exchanged with 1' molecules

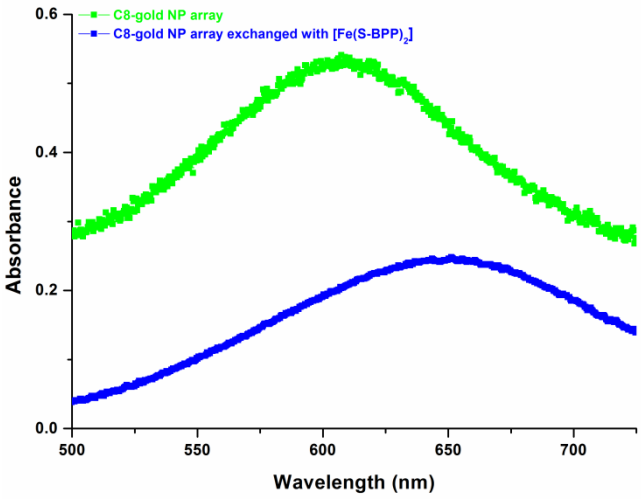

Figure C-2: UV-Vis absorption measurement of the surface plasmon resonance (SPR) peak in a single layer 2D **1'**-gold nanoparticle array on a glass substrate (see blue coloured spectra curve) compared with data from the same sample (see green coloured spectra curve) before the molecular exchange procedure.

To analyze the insertion of the conjugated **1'** molecules in the 2D C8-gold nanoparticles array by molecular exchange, ultraviolet-visible (UV-Vis) spectroscopy is used to confirm indeed that the **1'** molecules are introduced within the gold nanoparticle array. Microcontact-printed 2D alkanethiol-gold nanoparticle arrays, here stabilized by octanethiol (C8) molecules, exhibit a SPR absorption peak near 600 nm. After a molecular exchange process for four days the same sample is again analyzed by UV-Vis spectroscopy, indicating a red shift of the SPR peak (approximately ~40 nm) for a 2D **1'**-gold nanoparticles array. This confirms molecular exchange.

Appendix C.3

Temperature-dependent Raman measurements on bulk 1 SCO powder

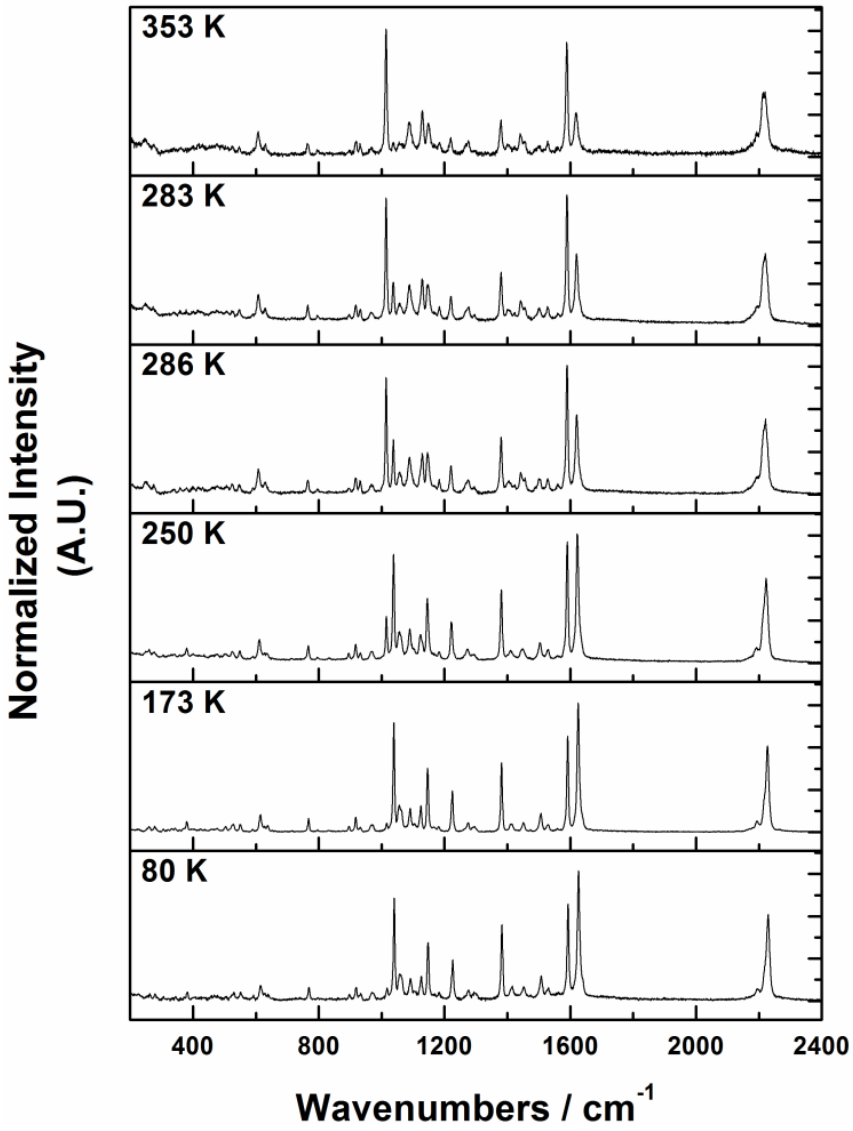

Figure C-3: Temperature-dependent Raman spectra of bulk **1** SCO powder excited at 785 nm (illuminating power 1.2 mw at the sample). The powder was kept for three hours at 80 K to ensure the SCO complex undergoes a complete spin crossover.

Temperature-dependent Raman measurements on bulk 1 SCO powder

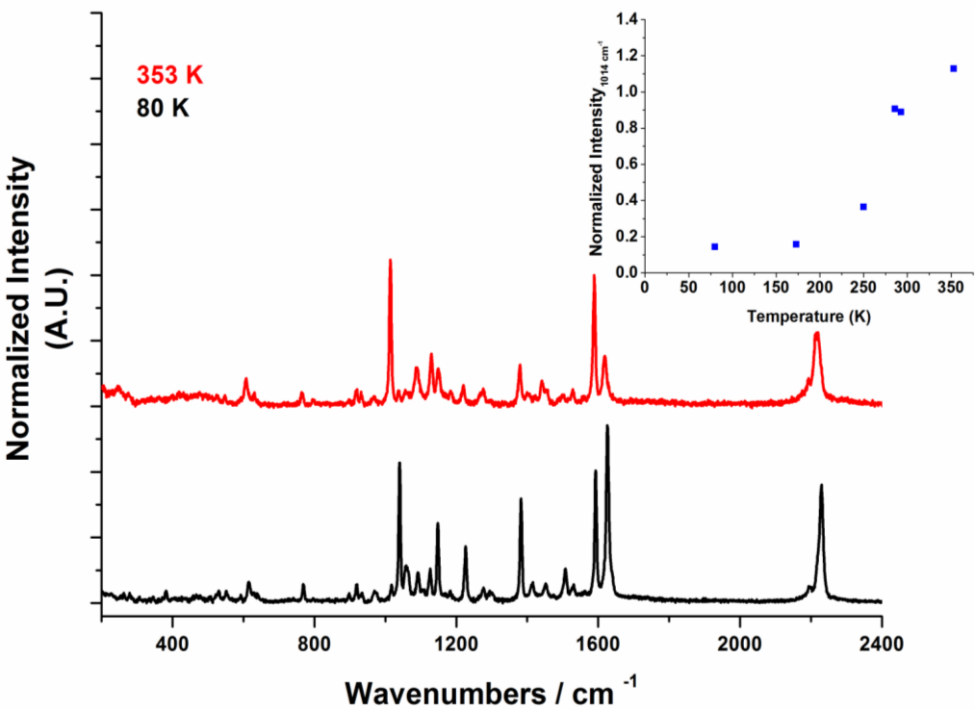

Figure C-4: Temperature-dependent Raman spectra of bulk **1** SCO powder sample at 353 K and 80 K excited at 633 nm (incident power 1.2 mW at the sample). Inset shows the intensity of mode at 1014 cm^{-1} (Pyridine ring breathing coupled Fe(II)-N str) as function of temperature normalized to 1592 cm^{-1} mode which showed weak temperature dependence. This is a qualitative indicator of the temperature-dependent spin transition taking place in the sample.

Temperature-dependent Raman measurements on bulk molecule 1 SCO powder

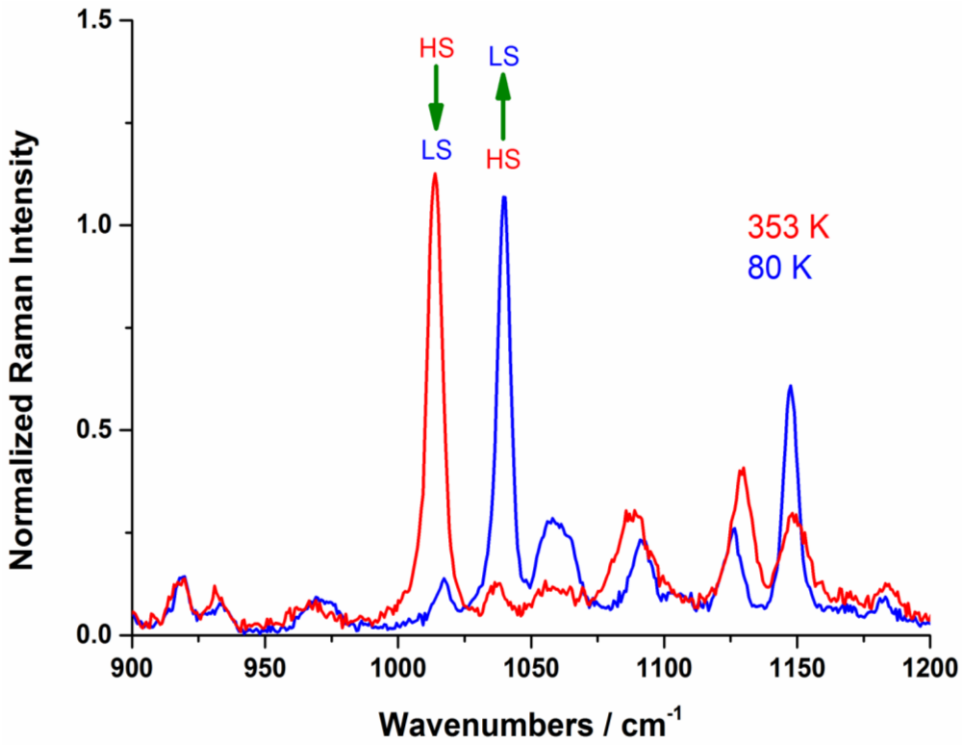

Figure C-5: Zoom in on Raman spectra of bulk molecule **1** SCO powder sample at 353 K and 80 K excited at 633 nm (incident power 1.2 mW at the sample). The intensity is normalized to 1592 cm^{-1} mode, which showed weak temperature dependence.

Appendix C.4

Temperature-dependent Raman measurements on 2D molecule 1'-gold nanoparticle array

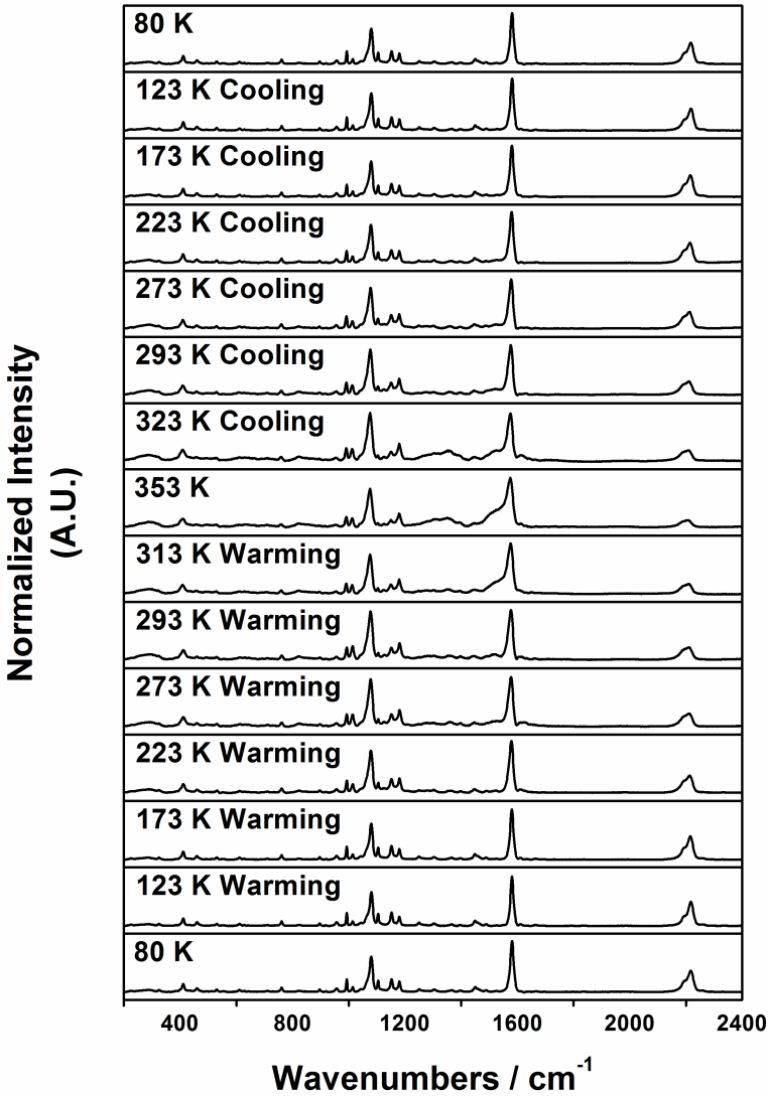

Figure C-6: Temperature-dependent Raman spectra of 2D molecule **1'**-gold nanoparticle array, excited at 633 nm (illuminating power 1.2 mW at the sample) on a quartz substrate.

Table 1: Selected key Raman peak assignments in high- and low-spin states

Raman Shift 1-Complex (cm^{-1}) HS	Raman Shift 1-Complex (cm^{-1}) LS	Raman Shift 1'- NP array (cm^{-1}) HS	Raman Shift 1'- NP array (cm^{-1}) LS	Assignment
-		321		Au-S mode
-		409 (s)	409 (s)	C-S str AT
990		990 (s)	990 (s)	AT in-plane ring-breathing mode,
1014	1039	1014	1035, 1014 (w)	Pyridine ring breathing coupled Fe(II)-N str
-	-	1076 (vs)	1080 (vs)	AT in-plane ring-breathing coupled to C-S stretch mode
1129	1125	1105	1125	in plane ring NCH str coupled to equatorial Fe-N str
1576 (w)	1576 (w)	1576 (s)	1580 (s)	AT in-plane C-C stretch
1589	1592	-	-	C=C str pyridine
1619	1626	1610 (w)	1633 (w)	C=C str pyrazine
2220 (s)	2229 (s)	2210 (s)	2216 (s)	alkyne C≡C stretch

- where AT is arylthiol moiety; ((v)s) is (very) sharp; str is stretch; (w) is wide

Where a Raman mode appears in SERS spectrum but not in the complex spectrum, it is because that feature is either obscured or exceedingly weak in the SERS spectrum.

Appendix C.5

Experimental part SQUID

The magnetic measurements were performed on a SQUID magnetometer (MPMS-XL-7 Quantum Design) at the Institute of Inorganic Chemistry, Technology and Materials in Bratislava. A multilayered (>3 layers) octanethiol-gold nanoparticles network without **1'** molecules (reference sample A) as well as two multilayered (>3 layers) gold nanoparticle networks with **1'** molecules (via molecular exchange) (Samples B and C) were each deposited on both sides of the quartz substrate (10 x 6 mm). Each sample was inserted into a plastic straw and fixed with tape to seal and to protect the samples (size microcontact printed array: ~ 5 x 5 mm on front side and also ~ 5 x 5 mm on backside of quartz substrate) from the surrounding environment. All herein reported magnetic measurements were carried out at 1 T external magnetic field in the temperature range 90-400 K. The temperature sweeping rate was 1 K min^{-1} and it was the same for cooling and heating modes. Magnetic data are represented as temperature dependence of magnetic moment.

Appendix C.6

A sample of a 1'-gold nanoparticle network that did not exhibit a resistance minimum

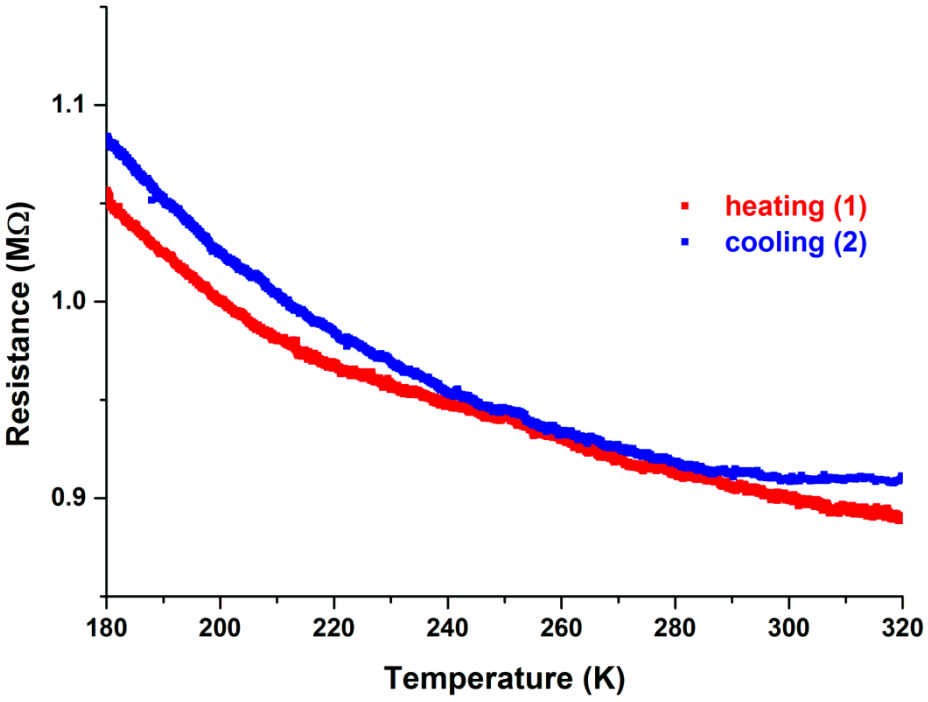

Figure C-7: *R-T* measurement of a molecule **1'**-gold nanoparticle network (stamped 3 times) where no minimum is exhibited. The first cycle is heating and the second cycle is cooling.